Earth Return Navigation Analysis for Manned Spacecraft Using Optical and Radiometric Measurements

Matthew J. Abrahamson* and Todd A. Ely+
Jet Propulsion Laboratory, California Institute of Technology, Pasadena, CA, 91109-8099

Future manned space missions will travel beyond low Earth orbit with more stringent navigation requirements and fewer navigation resources than used for the Apollo Program of the 1960s. A study has been performed to assess radiometric and optical tracking capabilities necessary to meet nominal and contingency Earth entry flight path angle requirements. Results indicate that 3 tracking stations will be insufficient for meeting nominal entry requirements, while the performance of a 6 station architecture is dependent on the entry geometry. Optical tracking results indicate that a narrow-angle camera is required for satisfying contingency Earth return requirements.

Nomenclature

EFPA	=	Earth entry flight path angle
TCM	=	trajectory correction maneuver
X_j	=	filter state vector at time t_j
Q_j	=	process noise matrix at time t_j
P_j	=	state covariance matrix at time t_j
$\Phi(t_{j+1}, t_j)$	=	discrete-time state transition matrix from time t_j to time t_{j+1}
x(t)	=	estimated filter parameters
p(t)	=	stochastic filter parameters
y(t)	=	considered filter parameters
$Q_{pp,j}$	=	process noise diagonal matrix for stochastic parameters at time t_j
$M(t_{j+1}, t_j)$	=	discrete-time Markov transition matrix from time t_j to time t_{j+1} for stochastic parameters
$I_{Ny \times Ny}$	=	identity matrix with dimension N_y by N_y
EI	=	Earth entry interface
WA	=	wide angle camera
NA	=	narrow angle camera
TLI	=	trans-lunar injection
TEI	=	trans-Earth injection
CFP	=	conceptual flight profile
MONTE	=	Mission-analysis, Operations, and Navigation Toolkit Environment

I. Introduction

On January 14, 2004, President George W. Bush articulated a new vision for space exploration that envisions the development of a safe and reliable transportation capability to and from all areas of the lunar surface with the ultimate goal of establishing a permanent manned presence on the Moon[1]. Much like the Apollo Program of the late 1960s, the new Constellation Program has been developing a transportation system that will ferry a crew of 4 to 6 astronauts to lunar orbit in a crew module and then maneuver down to the lunar surface using a lunar lander. Unlike Apollo, however, Constellation has plans to explore beyond the equatorial region of the Moon, provide substantial

* Staff Engineer, Guidance, Navigation, and Control Section, Jet Propulsion Laboratory, California Institute of Technology, MS 301-121, 4800 Oak Grove Drive, Pasadena, CA 91109-8099, AIAA Member. Email: Matthew.Abrahamson@jpl.nasa.gov.

+ Principal Engineer, Guidance, Navigation, and Control Section, Jet Propulsion Laboratory, California Institute of Technology, MS 301-121, 4800 Oak Grove Drive, Pasadena, CA 91109-8099, AIAA Senior Member. Email: Todd.A.Ely@jpl.nasa.gov.

autonomous capabilities, enable longer sorties, and meet the highest safety standards with fewer allocated resources. The Constellation-based crew module, dubbed Orion, must enable the exploration of all areas of the Moon with an inherent capability to execute a safe abort to Earth anywhere and at any time during the mission. The Constellation program plans to meet these stringent requirements with fewer tracking and recovery resources than were used for the Apollo program. This paper addresses two important GN&C requirements for Orion: (1) The ability to meet an Earth Entry Flight Path Angle (EFPA) requirement to enable a "skip entry" descent to a water landing and (2) the ability to safely navigate back to Earth in an abort scenario without communication to the ground ("No Comm"). Analysis of the first requirement involves considering several ground tracking architectures and evaluating their ability to meet the EFPA requirements, while analysis of the second requirement relies heavily upon onboard optical navigation techniques. Although the intended Constellation vehicle is Orion, the analysis considered here is generic to other manned spacecraft with similar Earth return requirements.

Recently, a review of the NASA manned spaceflight program by the Augustine Committee has recommended new goals for exploration beyond low Earth orbit, including visits to Lagrange points, asteroids, and other moons within the solar system. Regardless of the final direction, any manned mission beyond low Earth orbit must accomplish something not done since 1972: safe return of a manned spacecraft to Earth from beyond low Earth orbit. Implementation of a manned Earth return mission presents several unique challenges, primarily due to manned spacecraft exhibiting higher process noise characteristics (that result from vehicle venting and attitude control) than robotic spacecraft. Given the likelihood of fewer ground tracking assets as compared to Apollo, it is essential to examine the effect of various spacecraft noise levels on the ability to meet Earth entry requirements. In addition, potential missions to asteroids and other near Earth objects will rely heavily on optical navigation technologies similar to those presented in this paper because of modeling uncertainties associated with these destinations. Although the analysis in this paper focuses on specific Moon-to-Earth trajectories, the final conclusions are relevant to a host of potential missions beyond low Earth orbit.

II. Prior Work

The new vision for space exploration has sparked a renewed interest in lunar navigation studies over the past few years. D'Souza[2] examined the navigation performance of a modern era Apollo ground-tracking network consisting of twelve ground stations located around the globe providing 2-way and 3-way Doppler measurements. More recently, D'Souza et al.[3] examined the EFPA dispersions for various combinations of candidate ground-tracking stations by mapping the navigation knowledge at the final correction maneuver (TCM) to Earth interface (EI) using a state transition matrix. Moreau et al.[4] examined the benefits of incorporating GPS into the radiometric navigation solution and noted that non-gravitational accelerations present the most significant error source in the navigation solution. The analysis presented in this paper will examine a wider array of architecture options than considered previously with various stochastic process models for the non-gravitational accelerations wrapped into the EFPA mapping to EI.

With regard to abort scenarios, Zanetti[5] considered the performance of an onboard navigation system during a "No Comm" with the Earth ground system abort scenario. That is, the vehicle is unable to get navigation state updates from the ground, and must rely on onboard means to navigate. The primary measurement type used by Zanetti is a star-horizon measurement measured above the Earth's limb by an onboard star tracker during Earth return. The analysis within this paper will expand the analysis to include optical measurements of lunar landmarks, Earth-orbiters, and Earth limb points with new models for the optical sensors, the non-gravitational accelerations, and Earth limb variability.

III. Conceptual Flight Profiles

The analysis presented in this paper utilizes two conceptual flight profiles to simulate representative geometries to be encountered in a Constellation mission. Each flight profile simulates a 14-day roundtrip mission to the Moon with the intent to support a 7-day excursion on the lunar surface. Each trajectory departs Earth by executing a trans-lunar injection (TLI) burn, then coasts for 3.5 days before executing before performing a lunar orbit insertion (LOI) to achieve a 100 km circular lunar orbit. One trajectory uses a sequence of 3 maneuvers to perform LOI and the other uses only a single maneuver to directly insert into a 100 km orbit. Each trajectory orbits the Moon for approximately nine days, in order to simulate the accommodation of a seven-day surface expedition. Following the ninth day of orbiting the Moon, the spacecraft vehicle executes a set of three trans-Earth Injection (TEI) burns to

escape lunar orbit and return to Earth. Only the portion of the spacecraft trajectory from the final TEI burn (TEI-3) to the Earth entry interface (EI) will be considered in this paper.

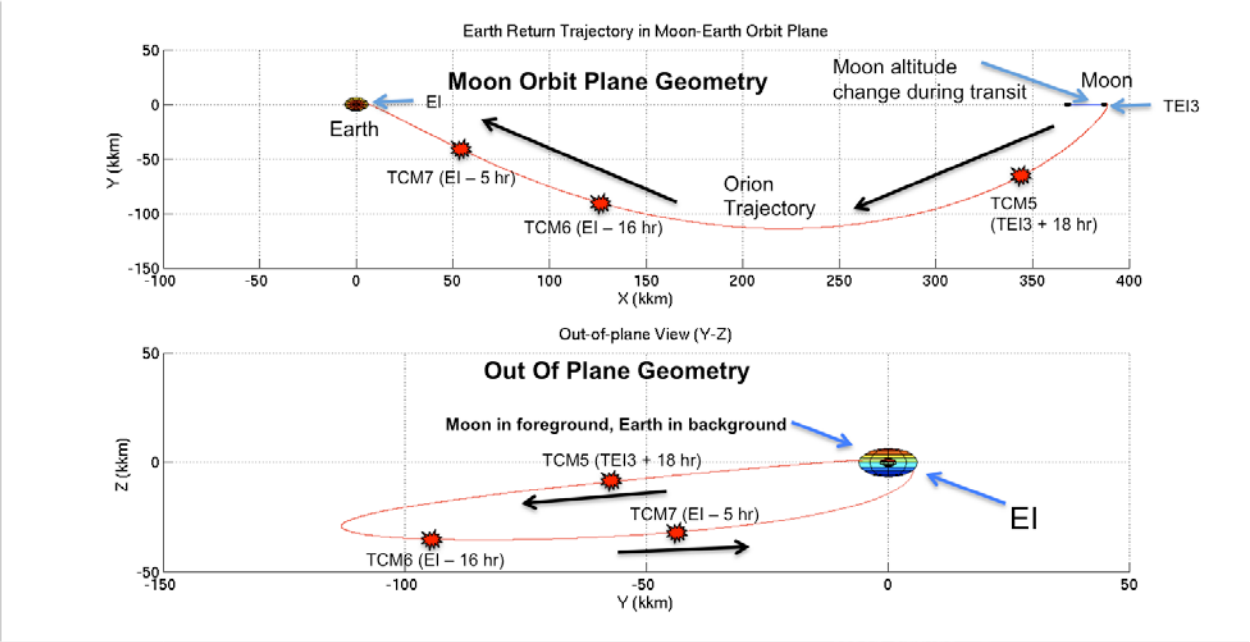

Figure 1: CFP-1 Trajectory Expressed In The Moon-Earth Orbiting Frame

A. Conceptual Flight Profile-1 (CFP-1)

The first trajectory to be considered, Conceptual Flight Profile-1 (CFP-1), simulates a representative mission to the mid-latitude regions of the Moon occurring in August 2018. The portion of CFP-1 to be considered in this study initiates at the final Trans-Earth Injection burn (TEI-3), at a lunar altitude of 265 km, and concludes at Earth Entry Interface (EI), defined at an altitude of 400,000 feet above the Earth's surface. The trajectory departs the Moon from a 149°-inclined orbit (retrograde) and approaches the Earth from the southern latitudes, eventually reaching EI over the northwest corner of Australia. At the time of TEI-3, the Moon is inclined 20.8° relative to the Earth equator at a distance of 386,784 km from the Earth's center.

Figure 1 illustrates the geometry of the CFP-1 trajectory relative to the Earth and Moon. The trajectory is plotted in the Moon orbiting plane, such that the x-axis is always aligned with the rotating Earth-Moon vector and the z-axis is aligned with the angular momentum of the Moon. CFP-1 can be seen to swing out a maximum of 120,000 km to the right of the Earth-Moon vector and up to 40,000 km below the Moon orbit plane during the transit back to Earth.

There are three trajectory correction maneuvers (TCMs) planned for execution during the Earth return. Figure 1 depicts the locations of these TCMs along the return trajectory. TCM5 occurs 18 hours after TEI-3 to clean up any errors from the TEI burns, while TCM6 and TCM7 are executed 16 hours and 5 hours before EI, respectively, to clean up errors accrued during Moon-Earth transit. For the purposes of this navigation analysis, it is assumed that each TCM will correct all spacecraft position and velocity dispersions down to the knowledge uncertainty, while adding uncertainties to the navigation solution due to burn execution errors. The final correction maneuver, TCM7, drives the EFPA dispersion observed at EI, which must be bounded such that it enables a skip entry descent that targets a precise landing in the Western United States. The current EFPA requirement is restricted to be no greater than 0.12 degrees (3-σ) dispersion at EI[3].

Figure 2 depicts the Earth ground track for the CFP-1 trajectory from TCM6 to TCM7. The trajectory can be seen to sweep over southeast Asia between TCM6 and TCM7, then swing around the horn of Africa prior to reaching Earth entry interface over the northwest corner of Australia. It can be observed in Figure 2 that the CFP-1 trajectory passes over potential tracking station locations in Australia, Japan, South Africa, and Guam. The tracking architectures depicted in Figure 2 will be discussed in section VI.

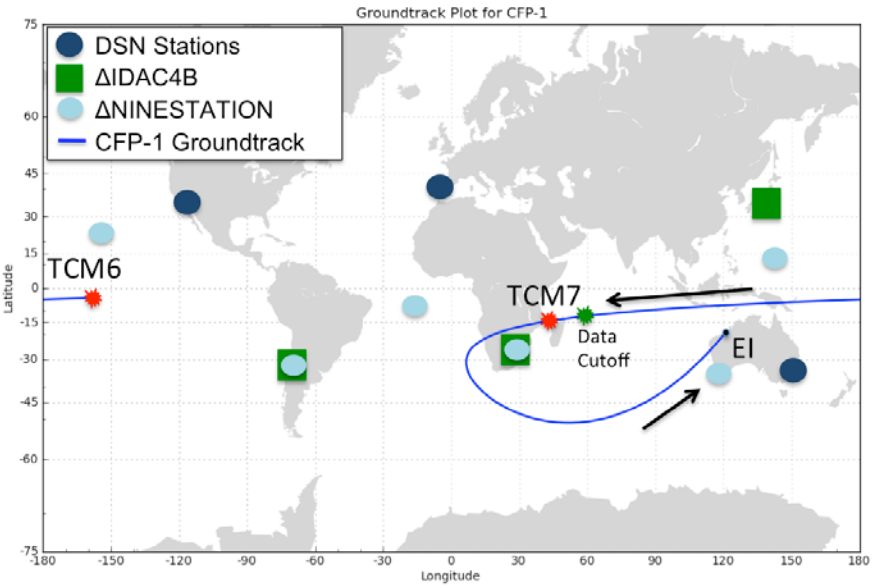

Figure 2: CFP-1 Trajectory Groundtrack From TCM6 to EI

B. Conceptual Flight Profile-1P (CFP-1P)

The second trajectory to be considered, Conceptual Flight Profile-1P (CFP-1P), simulates a representative mission to the polar regions of the lunar surface occurring in April 2024. The CFP-1P trajectory achieves a 100 km circular, 90°-inclined orbit to enable a 7-day surface stay in the polar regions of the Moon. The portion of the spacecraft trajectory to be considered here initiates at TEI-3 at an altitude of 2584 km above the lunar surface and inclination of 103° relative to the Moon and terminates at the Earth entry interface, 400,000 feet above the Pacific Ocean northeast of the Solomon Islands. At the time of TEI-3, the Moon orbit is inclined 28.5 degrees relative to the Earth equator at a distance of 360,396 km from the Earth.

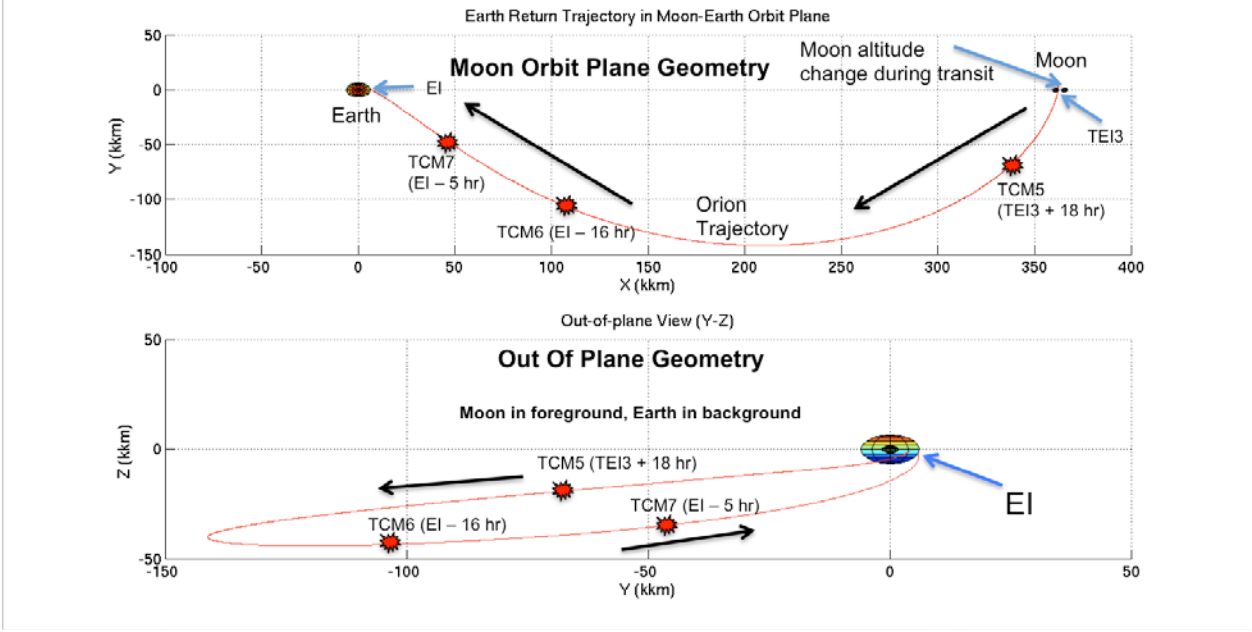

Figure 3: CFP-1P Trajectory Expressed In The Moon-Earth Orbiting Frame

Figure 3 depicts the relative placement of TCMs along the CFP-1P trajectory. As is the case for CFP-1, the three TCMs are executed 18 hours past TEI3, 16 hours prior to EI, and finally 5 hours prior to EI. In contrast to CFP-1, CFP-1P departs the Moon from a higher altitude and more highly inclined orbit and swings out a much greater distance to the right of the Earth-Moon vector during the return transit. Figure 4 depicts the CFP-1P trajectory ground track from TCM6 to EI. Unlike CFP-1, CFP-1P does not pass over the horn of Africa, reducing reliance on potential tracking stations in Africa and increasing the importance of the Australian and Japanese tracking stations. The CFP-1P trajectory reaches the Earth entry interface point over the southwest Pacific Ocean in order to target a skip entry profile for landing in the Western United States.

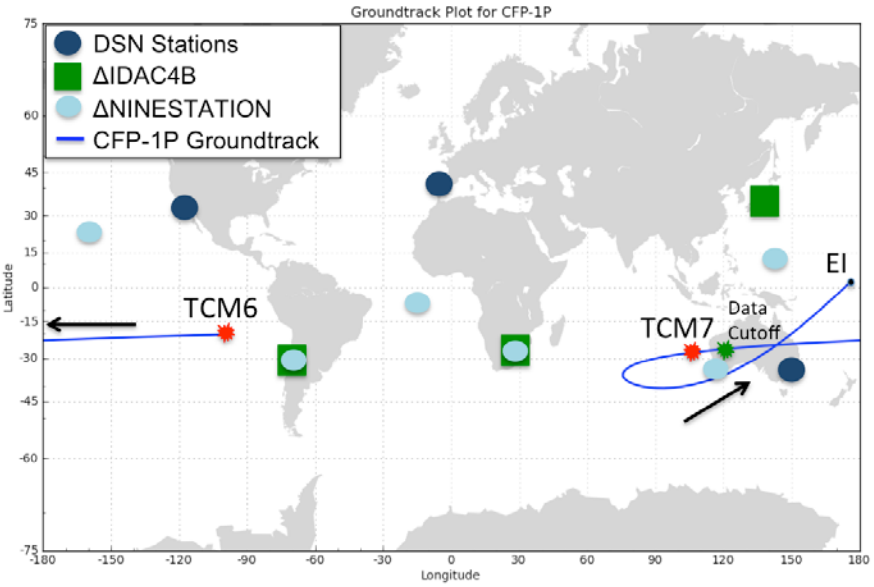

Figure 4: CFP-1P Trajectory Groundtrack From TCM6 to EI

IV. Navigation Analysis Tools

The analysis described in this paper uses a current state batch sequential, linear, UD-factorized Kalman filter for state determination. The navigation filter is part of JPL's integrated navigation toolkit called the Mission-analysis, Operations, and Navigation Toolkit Environment (MONTE), which provides a set of callable functions for the design, estimation, and control of spacecraft trajectories. MONTE relies on object-oriented programming, allowing users to construct object instances with a full set of callable functions. Python scripts drive the MONTE toolkit to configure and execute particular scenarios of interest. For this analysis, a Python-based tool called Lumina, developed by the co-author, is used to incorporate the CFP trajectories, simulate measurement observables, configure the filter to estimate the necessary parameters, establish the appropriate measurement models, and drive the filter propagation over the length of the trajectory.

These tools are used to perform linear covariance analysis, a methodology to obtain navigation performance statistics in a single run, rather than several Monte Carlo runs. The filter propagates a covariance matrix of state uncertainties forward in time via a state transition matrix, incorporates stochastic updates, and performs linearized measurement updates when measurements are obtained. Various stochastic processes, such as non-gravitational accelerations, are input to the solution as process noise at batch intervals. This capability enables several navigation architectures to be considered in a trade study without the time burden of a detailed Monte Carlo analysis.

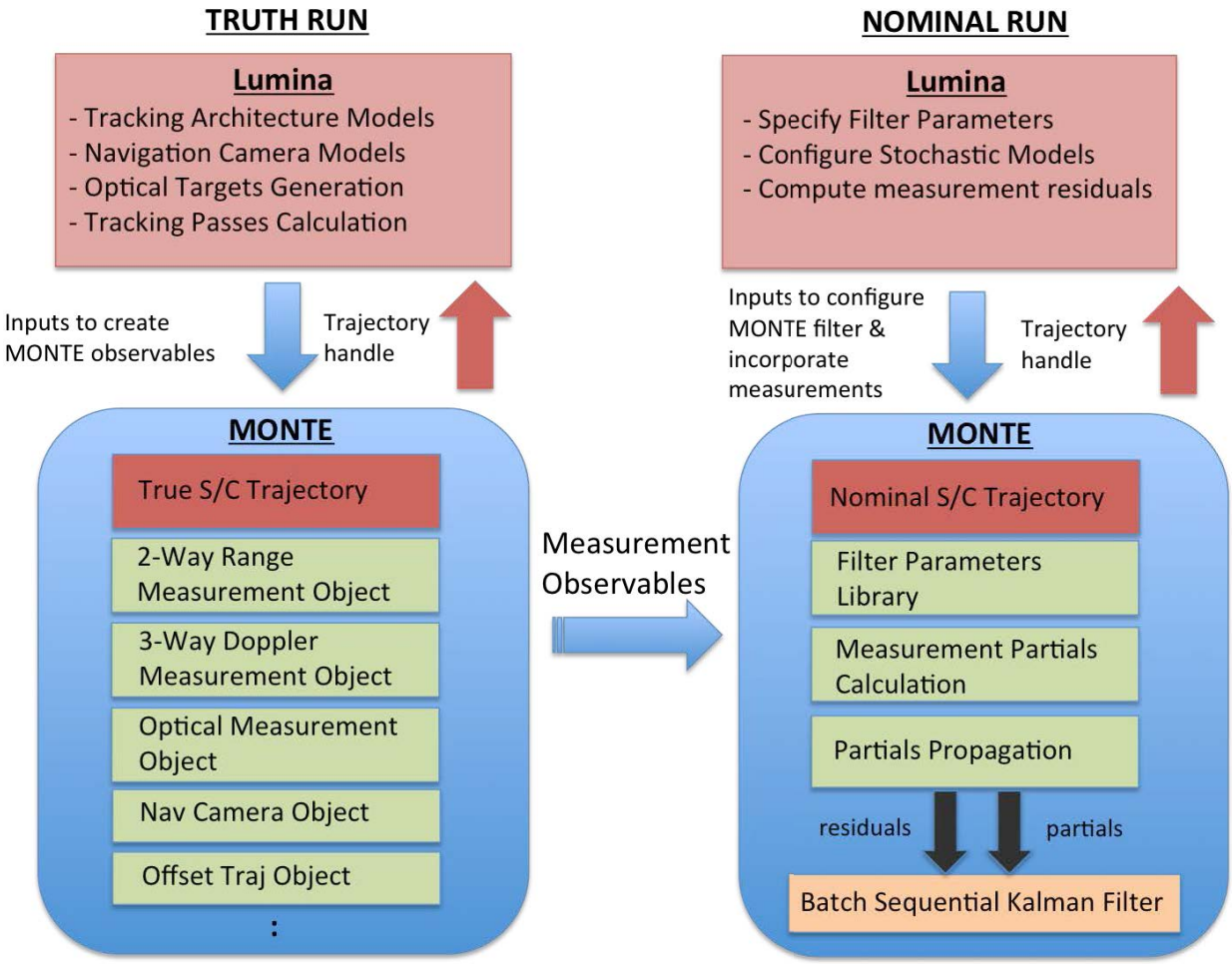

Figure 5: Lumina/MONTE Tool Interface

Figure 5 depicts the Lumina/MONTE interface. Lumina is used to establish models specific to a particular scenario, while MONTE provides generic functions for establishing particular object instances. In the scenarios investigated in this paper, Lumina calculates the tracking pass durations using the CFP trajectory, and then uses the set of pass intervals to create MONTE measurement objects. For example, when interpreting a pass showing both

Canberra and Usuda in the field of view, Lumina may construct a set of 2-way range measurement objects between Canberra and the spacecraft and/or a set of 3-way Doppler measurement objects between Canberra, Usuda, and the spacecraft. The MONTE objects contain important information, such as the observable measurement data, as well as important functions, such as computing the measurement partials and setting the measurement weight.

Lumina runs are executed in two phases. First, a truth run is executed with the purpose of establishing a set of measurement observables. As mentioned above, Lumina uses the CFP geometry to calculate a set of measurement passes, then constructs MONTE raw measurement objects. Once the truth run is complete, a nominal run is executed. The purpose of the nominal run is to construct the navigation filter blocks, configure the uncertainty parameters, propagate the navigation state covariance, and filter the measurement observables. Lumina specifies the uncertainty models and filter parameters required to initialize the MONTE navigation filter, then commands MONTE to calculate the measurement partial derivatives for the measurement objects created in the truth run, and finally commands the measurement updates to the MONTE filter.

A. Navigation Filter

The general discrete-time filter equations used in the MONTE filter are given by Bierman[9]:

Equation 1: Discrete-Time State Update

$$X_{j+1} = \Phi(t_{j+1}, t_j) X_j$$

Equation 2: Discrete-Time Covariance Update

$$P_{j+1} = \Phi(t_{j+1}, t_j) P_j \Phi(t_{j+1}, t_j)^T + Q_j$$

where

$$X_j = \begin{bmatrix} x(t_j) \\ p(t_j) \\ y(t_j) \end{bmatrix}, \qquad P_j = \begin{bmatrix} P_{xx_j} & P_{xp_j} & P_{xy_j} \\ P_{px_j} & P_{pp_j} & P_{py_j} \\ P_{yx_j} & P_{yp_j} & P_{yy_j} \end{bmatrix}, \qquad Q_j = \begin{bmatrix} 0 & 0 & 0 \\ 0 & Q_{pp_j} & 0 \\ 0 & 0 & 0 \end{bmatrix},$$

$$\Phi(t_{j+1}, t_j) = \begin{bmatrix} \Phi_{xx}(t_{j+1}, t_j) & \Phi_{xp}(t_{j+1}, t_j) & \Phi_{xy}(t_{j+1}, t_j) \\ 0 & M(t_{j+1}, t_j) & 0 \\ 0 & 0 & I_{Ny \times Ny} \end{bmatrix}$$

The navigation state vector is separated into three distinct categories: estimated parameters x(t), stochastic parameters p(t), and considered parameters y(t). Estimated parameters include both dynamic and bias parameters whose covariances may vary due to state transition matrix time updates (dynamic), but are not affected by process noise inputs Q_j. Stochastic parameters are parameters in the filter state that are allowed to change over a known time interval due to process noise. Process noise is applied to the stochastic parameters at regular intervals, called batches. The process noise models used for these parameters are first order Gauss-Markov, implemented in the diagonal matrices $M(t_{j+1},t_j)$ and $Q_{pp,j}$. The $M(t_{j+1},t_j)$ matrix represents the amount of correlation with the previous stochastic parameter estimates at time t_j, while $Q_{pp,j}$ represents the influx of new process noise at time t_j. The contributions from both components are combined in Equation 2 to update the stochastic parameter uncertainties at time t_{j+1}, prior to the next measurement update. The $M(t_{j+1},t_j)$ and $Q_{pp,j}$ matrices (both diagonal matrices – correlations between process noise parameters are not considered in this study) only have components that are active during stochastic updates when the corresponding stochastic parameters have a batch boundary at the time t_j. There are two types of stochastic parameters considered in this study. The first is a discrete white noise model with $M^k = 0$ and $Q^k_{pp} = \sigma^2$ for stochastic parameter k. The second is an exponentially correlated discrete random variable (ECRV) model with $M^k = e^{-\Delta t/\tau}$ and $Q^k_{pp} = \sigma^2(1 - e^{-2\Delta t/\tau})$ for stochastic parameter k. The time constant τ is the correlation time and the batch duration Δt is the update time. Note that in this formulation, the process noise Q_{pp} is exerted on the stochastic parameters rather than input directly to the dynamic variables, as is done with the typical

Kalman filter implementation. Lastly, considered parameters have uncertainties that influence the covariance of the filter solution, but have values that are held fixed and not estimated in the filter. Typically, these parameters represent physical quantities that cannot be adequately observed or modeled in the arc of data being used for the navigation study.

B. Uncertainty Models

The uncertainty models implemented in Lumina include environment uncertainties, spacecraft uncertainties, and measurement uncertainties. The environment and spacecraft uncertainty models will be discussed here, while the measurement uncertainties will be discussed in future sections detailing the radiometric and optical tracking architectures. Environmental uncertainties cover random variations present in the Earth's atmosphere, while the spacecraft uncertainties consist of initial position and velocity uncertainty, non-gravitational acceleration uncertainty, and burn execution error uncertainty.

1. Un-Fortunate Lack of Acceleration Knowledge (FLAK) Models

The lack of knowledge about small non-gravitational accelerations has become a particular difficulty for satisfying navigation requirements and has become colloquially known in the navigation community as "FLAK" (un-Fortunate Lack of Acceleration Knowledge)[3]. Contributions to FLAK include the periodic venting of the vehicle environmental control systems, attitude thruster firings, and waste dumps[3]. The presence of FLAK is a big nuisance to navigation estimation due to the fact that the acceleration levels are too small to be sensed by modern accelerometers, but are exerted over a long enough time period to drive large uncertainties in position and velocity knowledge. The FLAK levels used in this analysis are based on Apollo heritage that assumes a position uncertainty accumulation rate while in lunar orbit of 500 meters per hour (1σ) due to FLAK unmodeled accelerations[6]. An investigation of the process noise levels required to meet this error accumulation rate resulted in the FLAK values shown in Table 1[8]. The position uncertainty response to FLAK during Earth transit has been observed to exhibit one-third of the effect observed during lunar orbit[8]. The FLAK model includes both time intervals of active operation (active venting, crew operation, etc.), and time intervals of quiescent operation (crew sleep, non-venting, etc.). The quiescent operations are assumed to have FLAK levels one order of magnitude lower than in active operations.

Table 1: Position, Velocity, and Non-Gravitational Accelerations

Error Source	Parameter Type	A Priori Uncertainty (1σ)	Correlation Time	Update Time	Reasoning/Comments
Orion/Altair Assumptions					
Initial Position Uncertainties	Estimate	1000 km each component			
Initial Velocity Uncertainties	Estimate	10 km/s each component			
Non-gravitational Accelerations - Active	White Noise	1.725e-7 km/s^2 (steady state)	-	-	Active during crew activity periods which are opposite of the intervals specified below
Non-gravitational Accelerations - Quiet (White Noise Model)	White Noise	1.725e-8 km/s^2 (steady state)	-	-	Quiet during crew sleep periods consistent with current Ops Concept WG assumptions (10/6/08)

2. Burn Execution Models

The burn execution errors include both directional and magnitude errors in the delta-V achieved. The models considered in this study are identified in Table 2 and use a Gates model format[7]. The uncertainty associated with each burn is estimated as a bias parameter in the MONTE filter. The main engine model is used for the TEI3 burn, while the aux engine model covers TCM5 and TCM6. The TCM7 aux engine model is considerably less noisy since it is assumed to employ a reaction control system trim prior to execution.

Table 2: Burn Execution Error Models (1σ)

Error Type	Main Engine	Aux Engine	TCM7 Burn
Magnitude Additive	30 mm/sec	10 mm/sec	4 mm/sec
Magnitude Scale Factor	0.0167%	0.0167%	0.0167%
Direction Additive	10 mm/sec	6 mm/sec	4 mm/sec
Pointing	0.00064 rad	0.00064 rad	0.00064 rad
Filter Model	Bias in each direction of impulse	Bias in each direction of impulse	Bias in each direction of impulse

3. Environment Models

The environment uncertainties include variations in the Earth and Moon ephemerides, Earth and Moon gravity, Earth orientation, and Earth atmosphere. Many of these uncertainties directly impact the performance of the ground-tracking network. Table 3 dictates the environment uncertainty models used for this study.

Table 3: Environment Uncertainties

Error Source	Parameter Type	A Priori Uncertainty (1σ)	Correlation Time	Update Time
Environment				
Moon & Earth Ephemerides (SETIII parameters)	Considered	DE421 cov	–	–
Earth Pole X, Y	1st-order Gauss Markov stochastic	5 cm each component	48 hrs	6 hrs
Earth UT1	1st-order Gauss Markov stochastic	0.256 ms	48 hrs	6 hrs
Earth Ionosphere–day/night	1st-order Gauss Markov stochastic	55 cm/15 cm	6 hrs	1 hr
Earth Troposphere–wet/dry	1st-order Gauss Markov stochastic	1 cm/1 cm	6 hrs	1 hr
Earth Gravitational Constant (GM)	Considered	0.0014 km^3/sec^2	-	-
Moon Gravitational Constant (GM)	Considered	0.0001 km^3/sec^2	-	-

V. Entry Flight Path Angle Dispersions

The primary figure of merit considered in this study is the true EFPA dispersion from the nominal EFPA at Earth Entry Interface. The EFPA is defined as the angle between the velocity vector and the local horizontal plane at EI. The dispersion represents the statistical deviation (3σ) of the true EFPA from the nominal planned EFPA of the apriori trajectory at the time of entry. This differs from the navigation knowledge uncertainty, which is the statistical deviation of the true EFPA from the best estimate of the EFPA in the navigation filter at the time of entry. Unlike navigation knowledge, which can be improved instantaneously by incorporating new measurements, navigation dispersions are corrected by TCM burns.

In order to assess the navigation architecture's influence on the EFPA dispersion, the navigation knowledge uncertainty prior to the final TCM burn is considered. It is assumed in this study that each TCM corrects for all known trajectory dispersions down to the navigation knowledge level, but also contributes new trajectory errors due burn execution errors. The navigation knowledge uncertainty at the TCM data cut-off time is most relevant in this analysis, since this knowledge contains all of the information used to design the TCM burn. In this study, it is assumed that data cutoff occurs one hour prior to each TCM for computation and execution of the burn. This

knowledge uncertainty is mapped forward to EI, incorporating all stochastic processes encountered along the way, including burn execution errors and non-gravitational acceleration disturbances. This process is depicted in full detail in Figure 6. In order to assess the sensitivity of the final EFPA dispersion to the data cut-off time, this analysis will map the navigation knowledge at various times forward to EI.

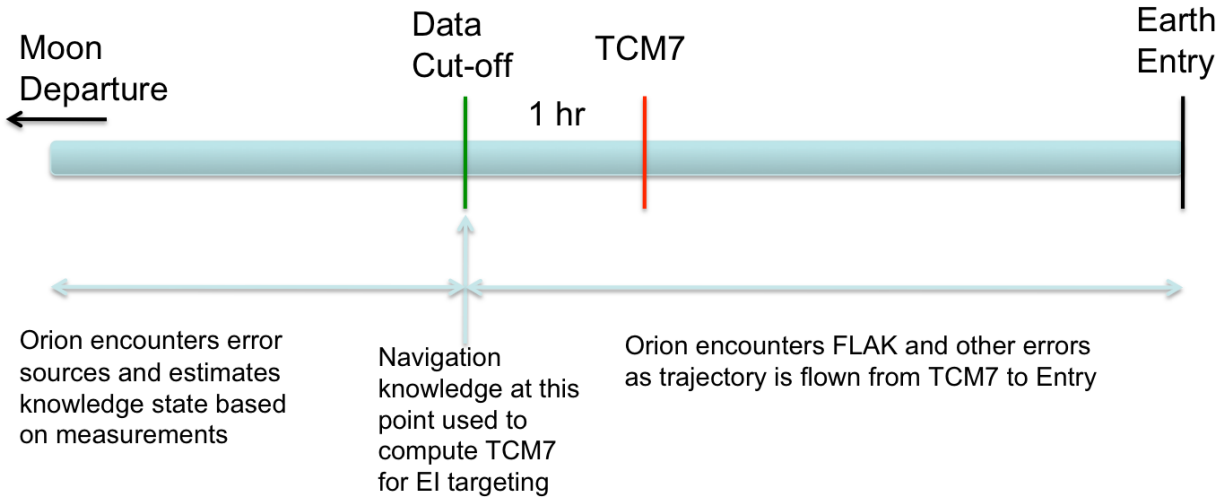

Figure 6: Entry Flight Path Angle Dispersion Calculation Methodology

VI. Radiometric Tracking Architectures

The first assessment of Earth return navigation performance will consider ground-based radiometric tracking architectures consisting of both existing and proposed ground stations around the Earth. The types of measurements considered here are 2-way range, 2-way Doppler, and 3-way Doppler measurements. The 2-way measurements contain data useful for estimating line-of-sight slant range and range rate to the spacecraft, while the 3-way Doppler measurement takes advantage of the geometry of a second tracking station to get crosstrack knowledge. The radiometric tracking is assumed to be continuous when there is a line-of-sight to the spacecraft above a 10° minimum elevation angle with the local horizon.

Figure 7: Radiometric Tracking Types

This paper analyzes the performance of three candidate ground tracking architectures. The base architecture is the Deep Space Network (DSN). The DSN is currently operational and provides navigation tracking for most deep

space spacecraft today. The second architecture, conceived during the IDAC4B[1] cycle, includes all DSN stations as primary stations and adds three proposed secondary stations for 3-way tracking with the primary stations. The addition of these stations provides a good North-South, East-West baseline of stations around the globe. This baseline is expected to provide strong geometry for 3-way radiometric measurements. The third proposed architecture, 9STATION, also includes the DSN as primary stations with six additional secondary stations for 3-way tracking with primary stations. The final architecture depicted in Figure 8 is the 12-station Apollo tracking architecture, which is included for comparison. Table 4 lists all of the stations modeled in this study, with the Apollo network listed for comparison.

Table 4: Proposed Radiometric Tracking Architectures

DSN	IDAC4B	NINESTATION	APOLLO
Goldstone, CA, USA	Goldstone, CA, USA	Goldstone, CA, USA	Goldstone, CA, USA
Canberra, Australia	Canberra, Australia	Canberra, Australia	Canberra, Australia
Madrid, Spain	Madrid, Spain	Madrid, Spain	Madrid, Spain
	Usuda, Japan	Dongara, Australia	Texas JSC, USA
	Hartebeestoek, South Africa	Hartebeestoek, South Africa	Florida KSC, USA
	Santiago, Chile	Santiago, Chile	Madagascar
		Hawaii	Hawaii
		Guam	Guam
		Ascension Island	Ascension Island
			Bermuda
			Carnarvon, Australia
			Canary Islands

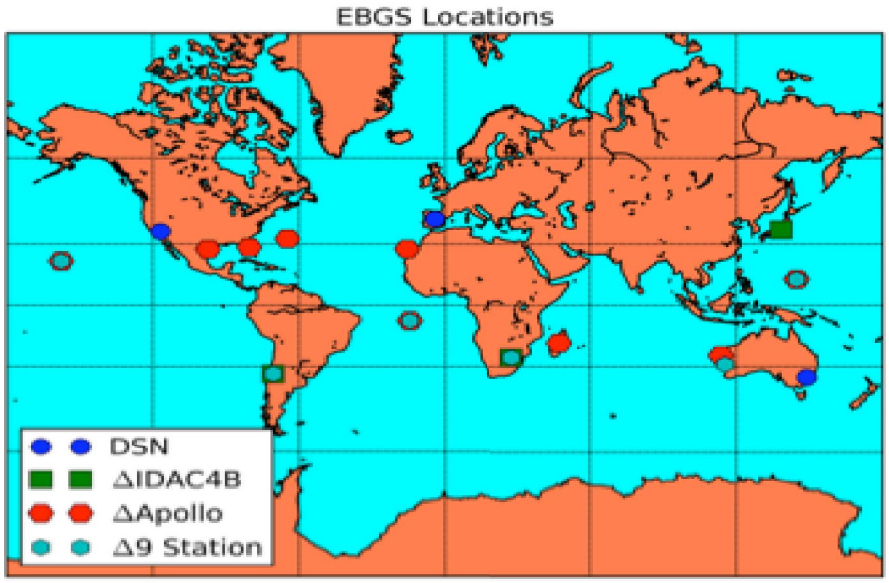

Figure 8: Earth-Based Ground Station Architectures

[1] Integrated Design Analysis Cycle 4B, Constellation Flight Performance Systems Integration Group

Table 5 contains the error models used for the radiometric measurements. The random biases present in the 3-Way Doppler and 2-way range measurements are modeled as white noise processes in the MONTE filter. In addition, the uncertainty of the ground station locations due to tidal loads and drifts is modeled as consider variables in the MONTE filter. Lastly, the measurement noise is given for 2-way range, 2-way Doppler, and 3-way Doppler measurements.

Table 5: Radiometric Error Models

Error Source	Parameter Type	A Priori Uncertainty (1σ)	Correlation Time	Update Time
Earth Ground Network - Spec Levels				
S-Band 2/3-way Doppler Noise	–	0.674 mm/s @ 60 Sec	–	–
S-Band 3-Way Doppler Bias	White Noise	0.3 mm/s	–	Per pass
S-Band 2-way Range Noise	–	6.5 ns (~ 1.95 m)	–	–
S-Band 2-Way Range Bias	White Noise	6.5 ns (~ 1.95 m)	–	Per pass
Station Locations	Consider	10 cm	–	–

VII. Optical Tracking Architectures

The second assessment of Earth return navigation performance will consider onboard optical tracking architectures consisting of both Earth-based and Moon-based targets. These scenarios will simulate the performance of onboard navigation estimation as opposed to ground-based navigation estimation for radiometric tracking. An onboard navigation capability will be vital for contingency scenarios in which communication with the ground is lost. Several optical targets, such as lunar landmarks, Earth orbiting satellites, and Earth limb points will be considered here.

A. Optical Targets

1. Lunar Landmarks

A maximum of 100 lunar landmarks are randomly generated for each optical picture containing the Moon, with a maximum of 10 landmarks lying on the sunlit portion of the Moon selected as observables. The randomly generated lunar landmarks are uniformly distributed over the camera field of view. The pixel/line values of the observable landmarks are converted to MONTE objects in the Moon body-fixed frame for generation of optical point measurements.

Table 6: Landmark Target Model

Landmark Parameters	
Parameter	**Value**
Maximum Landmarks Per Picture	10
Distribution	Uniform random in camera FOV
Landmarks Sunlit	Yes

2. Earth Orbiting Satellites

Four Earth-orbiting satellites in geostationary orbit are included for optical tracking during Earth return. The objects are equally spaced by 90° in the orbit about the Earth. During the Earth return, the camera pointing alternates

between satellites at measurement batch boundaries. It is assumed that the onboard computer has been preloaded with ephemeris models of select geostationary satellites, so orbit errors are not modeled in this study.

Table 7: Earth Orbiting Satellites Model

Earth Satellites	
Number of objects	4
Inclination	0
Eccentricity	0
Altitude	36,000 km
Measurements	Alternate between SATs at picture batch boundaries

3. Earth Limb Point Measurements

A set of up to 24 target points along the limb of the Earth will be observed during Earth return. The limb points are equally spaced by 15° along the edge of the Earth in the camera focal plane for each picture. The limb points lying on a sunlit portion of the Earth are captured as observables, while limb points lying in the dark areas are discarded. Figures 9 and 10 depict the limb target generation process, with **A** representing the spacecraft to Earth center vector and **p** representing the plane perpendicular to **A**.

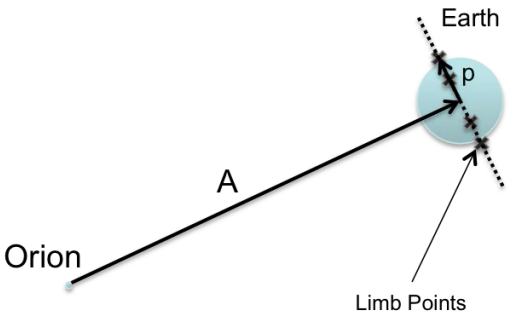

Figure 9: Limb Target Model

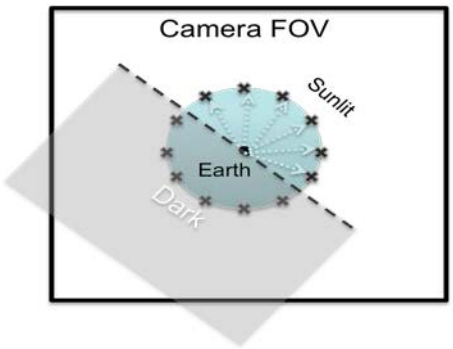

Figure 10: Focal Plane View

B. Camera Models

Since the Earth return geometry includes tracking of objects at both short and long ranges, this study will consider both a wide-angle (WA) camera model and a narrow-angle (NA) camera model. The wide-angle camera is intended to simulate startracker-level performance in a contingency abort scenario. The narrow-angle camera is intended to simulate the placement of a dedicated gimbaled optical navigation instrument on the spacecraft, similar to the proposed dual-axis instrument shown in Figure 11. The dual-axis gimbaled instrument would be ideal for many deep space applications, with a wide-angle camera able to provide a large FOV at short ranges (e.g. orbit) and a narrow angle camera available for long range tracking (e.g. transit). Only the latter camera in the dual-axis instrument will be considered here.

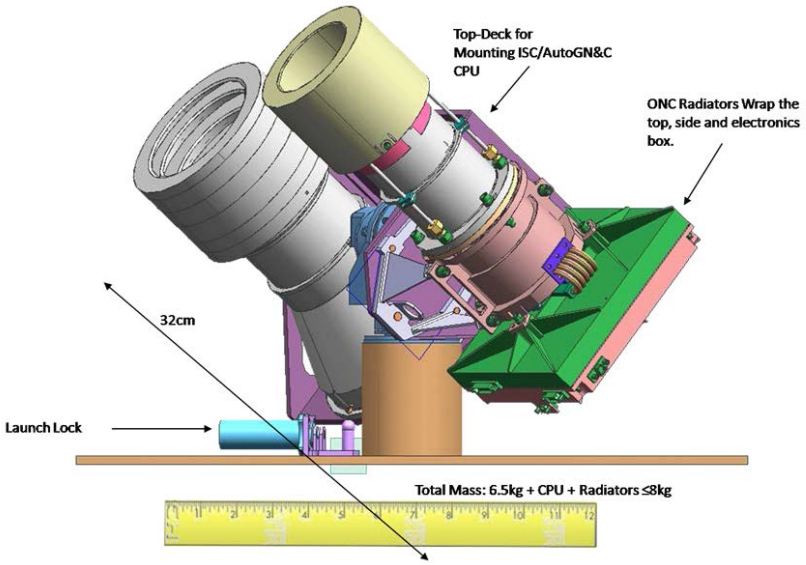

Figure 11: Proposed Optical Navigation Instrument

The wide-angle camera model provides a 21° field of view for acquisition and measurement of optical targets. The narrow-angle camera model provides a 1.4° field of view, similar to a high definition imager on the Mars Reconnaissance Orbiter. The optical parameters for each camera are given in Table 8.

Table 8: Navigation Camera Models

Optical Navigation Cameras					
Camera	Type	Focal Length	Pixel/Line Center	Pixel/Line Limits	K-matrix (pixels/mm)
Wide-Angle Camera	Startracker	33.9 mm	(256.5, 256.5)	(0.5 512.5)	[41.5 0 0 0 41.5 0]
Dual-Head Instrument	Narrow Angle	500 mm	(512.5, 512.5)	(0.5, 1024.5)	[83.3333 0 0 0 83.3428 0]

This study will consider both gimbaled-axis and fixed-axis options for each camera. For the fixed-axis model, it is assumed that optical pictures can only be acquired every 12 hours, due to the need for an attitude maneuver to modify the camera boresight. For this model, a batch of 60 pictures is observed at a rate of 1 picture per minute every 12 hours. For the gimbaled-axis model, it is assumed that a two-axis gimbal is will continuously point the camera at the desired optical target. For this model, a batch of 30 pictures is observed at a rate of 1 picture per minute every hour. In addition to these imaging intervals, additional images are observed at a rate of 1 picture per minute for two hours prior to each TCM data cutoff time.

Table 9: Optical Measurement Frequencies

Measurement Frequency	
Scenario	Measurement Model
Fixed-Axis	Batch of 60 pictures every 12 hours 1 picture/min
Gimbaled-Axis	Batch of 30 pictures every hour 1 picture/min
Special Considerations	1 picture/min from TCM - 3 hours to TCM - 1 hour For all TCMs

The pointing frame of the camera is constructed using unit vectors to reference bodies. For this analysis, the azimuth and elevation of the camera boresight is measured relative to a reference frame called the roll-celestial frame. The roll-celestial frame is constructed based upon the Sun and Earth vectors, as described in Table 10. The transformation to the camera frame involves rotating about the z and y-axes by the azimuth and elevation angles of the optical target vector, aligning the z-axis along the spacecraft to target vector.

Table 10: Camera Pointing Frames

Camera Pointing			
Direction	Pointing	Frame Axis	Notes
Roll Reference	Sun	Z-axis Roll-Celestial Frame	Roll-Celestial Frame transforms to Camera Frame by rotation about the Z and Y axes by Azimuth and Elevation of Camera boresight vector, respectively.
Clock Reference	Earth	Determines X-Z plane in Roll-Celestial Frame	
Camera Boresight	Moon Center	Z-axis Camera Frame	

The x and y-axes of the camera frame represent the sample and line coordinates of the optical measurement observables. All optical measurements will be recorded as a (pixel, line) point for inclusion in the navigation filter, as depicted in Figure 12.

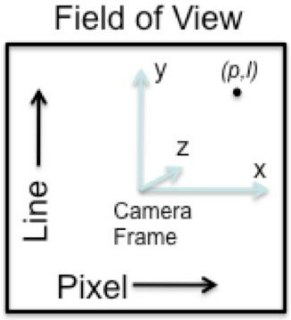

Figure 12: Depiction of Camera Focal Plane

C. Uncertainty Models

The uncertainty models for the optical measurements include both systematic errors (e.g. target location) and measurement errors (e.g. instrument noise). The measurement noise of both camera models is 0.1 pixels (1σ) for optical point measurements, but increases to 0.33 pixels (1σ) for limb measurements due to difficulty extracting observables from a hazy, variable atmosphere. A white noise model is used to simulate camera pointing uncertainty. For both cameras, it is assumed that the levels of pointing uncertainty shown in Table 11 are achieved by observation of the star fields and estimation in the navigation filter. The actual attitude estimation process is not included in this study. Lastly, an uncertainty in the location of the Earth limb is included due to atmospheric irregularity and variability. The limb of the Earth varies based on time of day, weather events, seasonal effects, longitude, latitude, and even the Sun cycle. Due to the difficulty of modeling this variability, the uncertainty in the limb position is designated as a considered parameter in the navigation filter.

Table 11: Optical Uncertainty Models

Optical Navigation Error Sources					
Error Source	**Parameter Type**	**A Priori Uncertainty (1σ)**	**Correlation Time**	**Update Time**	**Reasoning/Comments**
Attitude Pointing Errors	White Noise	0.1 mrad in RA, DEC, TWIST for Wide Angle Camera/Startracker 3 microradians in RA, DEC, TWIST for Narrow Angle Camera	-	60 sec	Camera platform random pointing error
Navigation Camera Measurement Noise	--	0.1 pixel in pixel and line components for Wide Angle Camera/Startracker (point measurements) 0.1 pixel in pixel and line components for Narrow Angle Camera (point measurements) 0.33 pixel for all limb measurements	-	Per optical measurement	Uncertainty in the sample and line coordinates recorded by the camera
Earth Limb Error	Consider	10 km each component	-	-	Uncertainty in Earth limb location due to atmospheric variability

VIII. Results

A. Radiometric Tracking Results

1. CFP-1 Results

Figure 13 shows the EFPA dispersions calculated when mapping the navigation solution at the nominal TCM7 data cutoff time (TCM7-1hr) forward to EI. For each of the three proposed architectures, five levels of FLAK are investigated to examine the EFPA dispersion sensitivity to FLAK disturbances encountered both before and after the TCM7 data cutoff.

1. No FLAK encountered during the entire Earth return scenario
2. Only quiet levels of FLAK encountered during the entire Earth return scenario
3. Nominal active/quiet FLAK cycles prior to TCM7 data cutoff; No FLAK encountered after TCM7 data cutoff
4. Nominal active/quiet FLAK cycles prior to TCM7 data cutoff; Quiet FLAK encountered after TCM7 data cutoff
5. Nominal active/quiet FLAK cycles prior to TCM7 data cutoff; Active FLAK encountered after TCM7 data cutoff

Nominally, the FLAK considered in this study exhibits alternating periods of active and quiet FLAK corresponding to the crew sleep cycles. The time period from the TCM7 data cutoff time to EI (reentry) is constrained to have quiet levels of FLAK in the nominal scenario (purple bar). If the time period from TCM7 data cutoff to EI were to exhibit active levels of FLAK rather than quiet levels, the EFPA dispersions represented by the red bars would be observed. Similarly, the yellow bar examines the scenario in which FLAK levels are effectively zero from TCM7 data cutoff to EI. The remaining two cases examine the EFPA dispersions in the absence of any FLAK throughout the entire Earth return (green bar) and in the case of only quiet FLAK levels exhibited throughout the entire Earth return. Cases 1 and 3 are only examined here to provide a benchmark for examining the EFPA sensitivity to FLAK. It is unrealistic to expect any periods of absolutely zero FLAK exposure during Earth return. Therefore, cases 2, 4, and 5 will provide potential performance numbers for each tracking architecture, while cases 1 and 3 will serve as benchmarks for comparison.

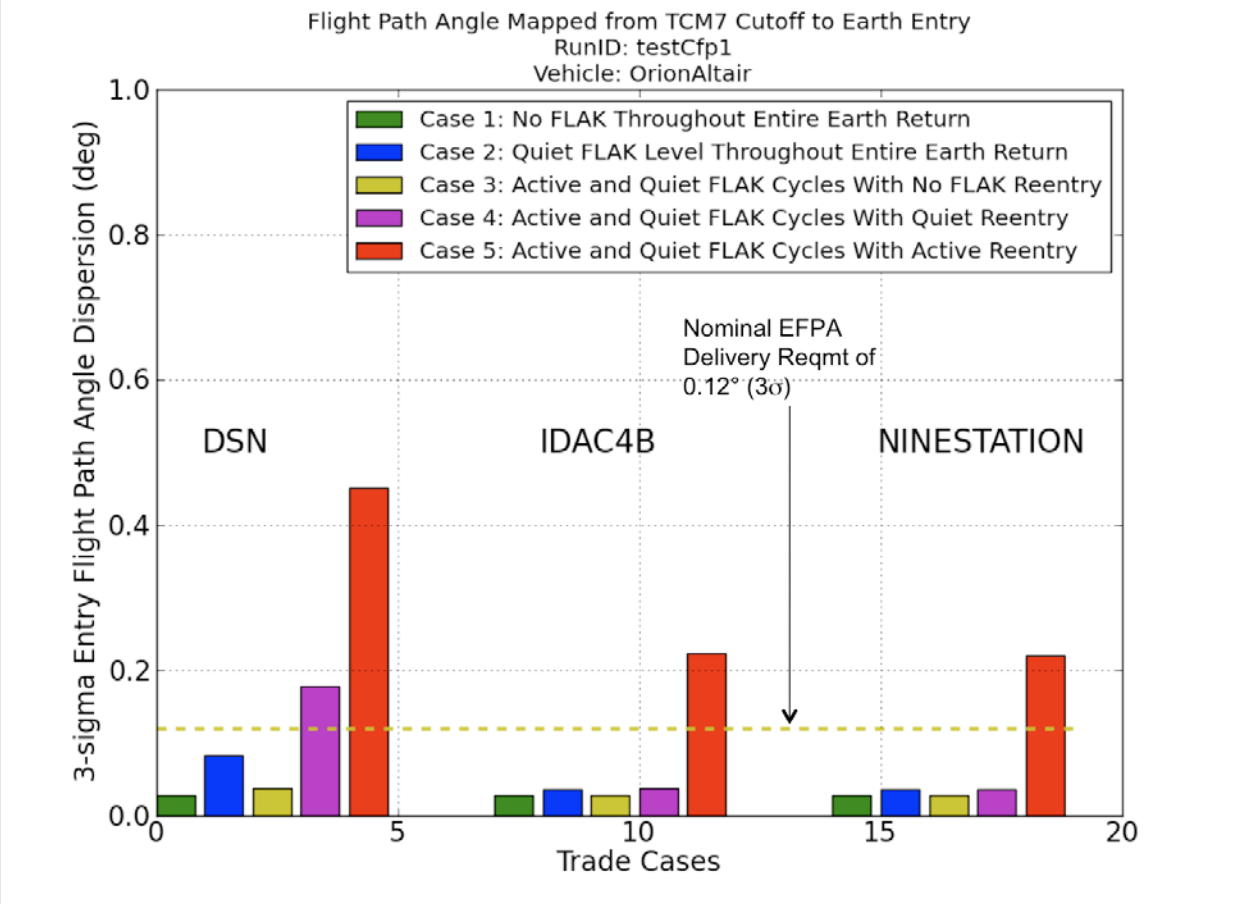

Figure 13: 3σ CFP-1 EFPA Dispersions For Various Tracking Architectures & FLAK Levels

Results indicate that a DSN-only tracking network will be insufficient for achieving the EFPA requirement of 0.12° if active and quiet cycles occur prior to TCM7 cutoff, regardless of the FLAK level after TCM7 cutoff. By comparing cases 2 and 4, it is observed that the EFPA dispersion is nearly doubled when active FLAK cycles are inserted prior to TCM7 cutoff. This implies that the DSN lacks sufficient tracking to minimize the effect of active FLAK on the navigation knowledge prior to TCM7 cutoff. It can be observed that the DSN architecture exhibits high sensitivity to FLAK encountered both before TCM7 cutoff and after TCM7 cutoff. The sensitivity to pre-TCM7 cutoff FLAK can be seen by comparing cases 1 and 3. The final EFPA more than doubles when active and quiet FLAK cycles are inserted prior to the TCM7 cutoff. However, both cases still remain within the requirement threshold. If case 4 is then compared to case 3, it can be seen that the EFPA dispersion increases by a factor of 5 when quiet levels of FLAK are inserted post-TCM7 cutoff. If cases 3 and 5 are compared, a factor of 13 increase is observed when active levels of FLAK are included. In these last two cases, it is difficult to extract the influence of the TCM7 cutoff navigation knowledge from the influence of the post-TCM7 cutoff FLAK. These considerations can be investigated by comparing the DSN architecture results with the results from IDAC4B and NINESTATION exhibiting greater tracking capabilities.

When comparing the DSN architecture results to the IDAC4B and NINESTATION results, it is observed that all cases have reduced EFPA dispersions for the latter architectures except for case 1. Since additional tracking can only benefit the navigation knowledge prior to the TCM7 data cutoff, this indicates an insufficient amount of tracking in the DSN architecture to achieve a good navigation state fix prior to designing the TCM7 burn. This point is further emphasized by observing that the IDAC4B and NINESTATION results are nearly identical for all FLAK cases. This indicates that both IDAC4B and NINESTATION have sufficient tracking resources to minimize navigation knowledge uncertainty prior to the TCM7 data cutoff, and the EFPA dispersions are primarily driven by post-TCM7 cutoff FLAK.

Figure 14 shows EFPA dispersions results mapped forward from various data cutoff times. It can be observed that IDAC4B and NINESTATION architectures result in identical EFPA dispersions if the TCM7 data cutoff time is

within 9 hours of EI. The two results converge with the addition of Canberra-Hartebeesthoek 3-way measurements to the IDAC4B solution. Although the DSN cases 4 and 5 do not satisfy the EFPA requirements with the nominal TCM7 data cutoff time, the results can be greatly improved if the TCM7 cutoff is moved 1 hour closer to EI due to the inclusion of Madrid 2-way measurements in the navigation solution. However, moving TCM7 closer to EI requires an increase in the TCM7 delta-V budget.

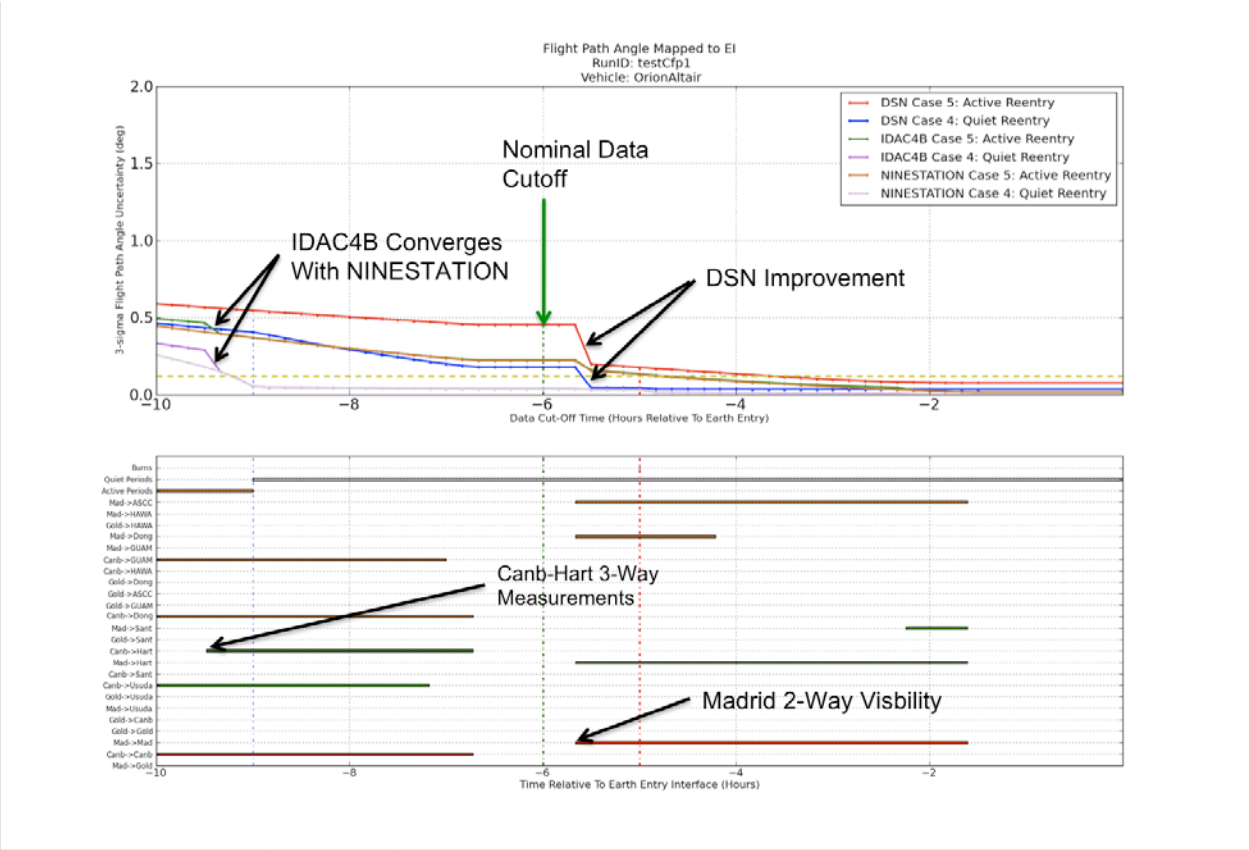

Figure 14: 3-Sigma EFPA Mapping From Various Data Cutoff Times For CFP-1 Radiometric Cases

The IDAC4B architecture passes the requirement with significant margin except for the case assuming "active" FLAK levels from TCM7 to EI. Since this FLAK is encountered after the TCM7 maneuver design and execution, additional tracking stations cannot provide any benefit. This can be confirmed by observing that the 9STATION architecture results are nearly identical to the IDAC4B results. In other words, there is sufficient tracking to narrow the TCM7 design knowledge as much as possible and the FLAK encountered between TCM7 and EI is driving the EFPA dispersions. Either TCM7 can be moved closer to EI or a requirement must be levied on the spacecraft to guarantee a quiescent level of FLAK from TCM7 to EI.

The following conclusions can be drawn from this trade comparison:

1. The DSN-only tracking architecture lacks sufficient tracking resources to confidently meet EFPA requirements, but results can be improved by moving TCM7 closer to EI.
2. The IDAC4B and NINESTATION architectures have sufficient tracking to minimize navigation knowledge errors at TCM7 data cutoff, but are adversely affected by FLAK encountered in the reentry phase.
3. The ability to meet the EFPA requirement is highly dependent on the ability of the spacecraft to minimize FLAK disturbances from TCM7 data cutoff to EI.

2. CFP-1P Results

A similar FLAK trade was performed for the CFP-1P trajectory to assess the influence of geometry variations on the EFPA dispersion. Figure 15 shows the EFPA dispersion results for the three proposed tracking architectures and five FLAK levels. Overall, many of the trends observed in the CFP-1 results still remain, with some differences in the IDAC4B results.

The conclusions made in the previous section regarding the DSN architecture performance still apply to the CFP-1P case. As observed in Figure 15, DSN cases 4 and 5 do not yield acceptable EFPA results. The combination of poor tracking performance pre-TCM7 data cutoff, combined with the effect of FLAK disturbances post-TCM7 results in poor EFPA targeting. The geometry variation presented in CFP-1P did not have any pronounced effect on the DSN results.

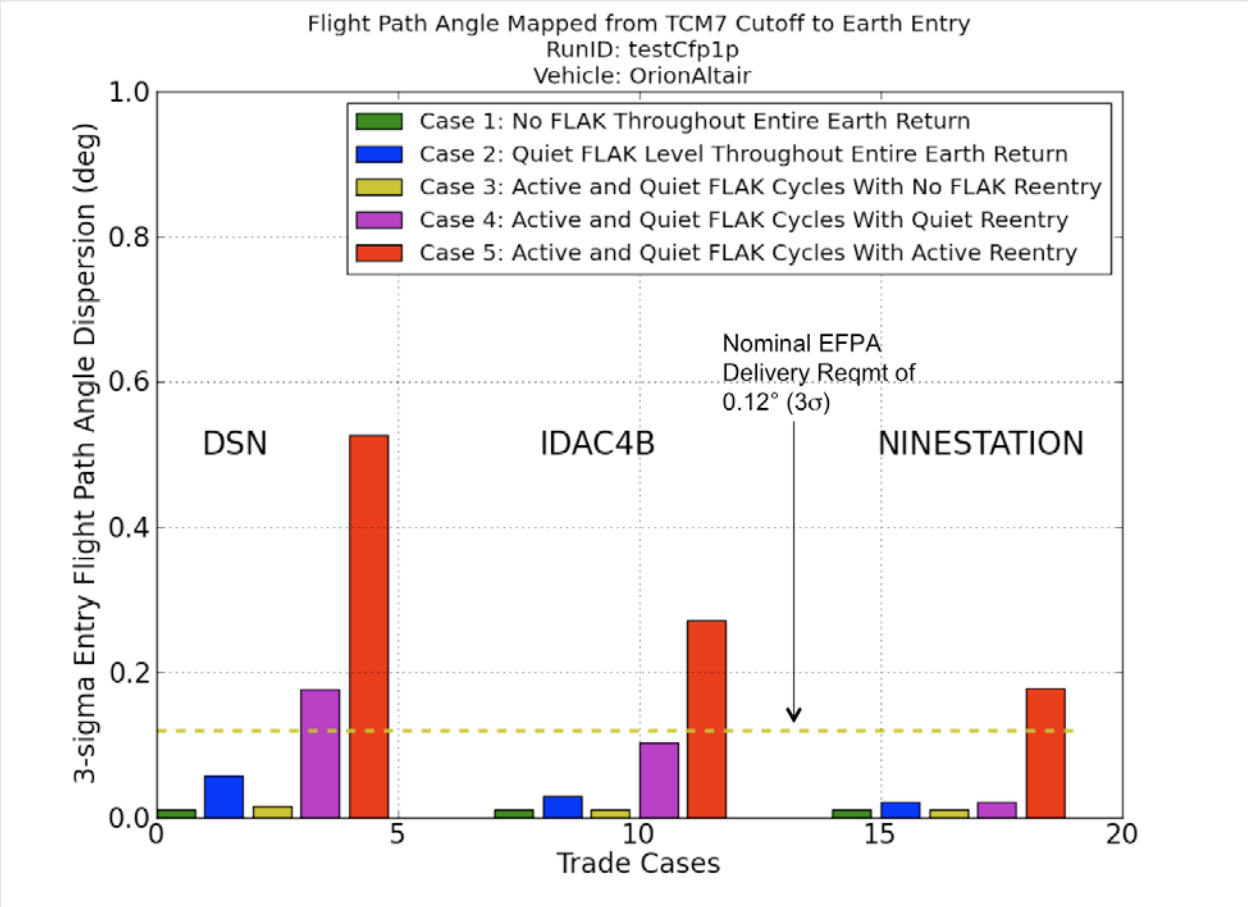

Figure 15: CFP-1P EFPA Dispersion Results For Various FLAK Levels

Similarly, the NINESTATION results for CFP-1P are nearly identical to the CFP-1 results. In fact, the geometry appears to slightly enhance the tracking performance, resulting in slightly lower EFPA dispersions. The only case exceeding the EFPA requirement exhibits an active level of FLAK from TCM7 data cutoff to EI. Again, this places extra importance on future FLAK characterization and investigation.

In contrast to the CFP-1 results, the CFP-1P results indicate a marked difference between IDAC4B and NINESTATION performance. For the CFP-1P scenario, the IDAC4B architecture is barely able to meet the EFPA requirement for case 4, while this case was easily met for CFP-1. While the CFP-1 results suggested that the IDAC4B tracking set would be acceptable for a vehicle in quiet FLAK mode prior to reentry with large margin, the CFP-1P results imply that the additional tracking stations in the NINESTATION configuration can significantly enhance performance. Figure 16 explains the difference in tracking performance. While the IDAC4B architecture in CFP-1 was able to provide Canberra-Hartebeestoek observations nine hours prior to EI, these observations are not visible by the CFP-1P trajectory until after the nominal data cutoff time. As with the DSN cases in CFP-1, the EFPA performance can be significantly improved by moving TCM7 closer to EI, but will result in a delta-V penalty.

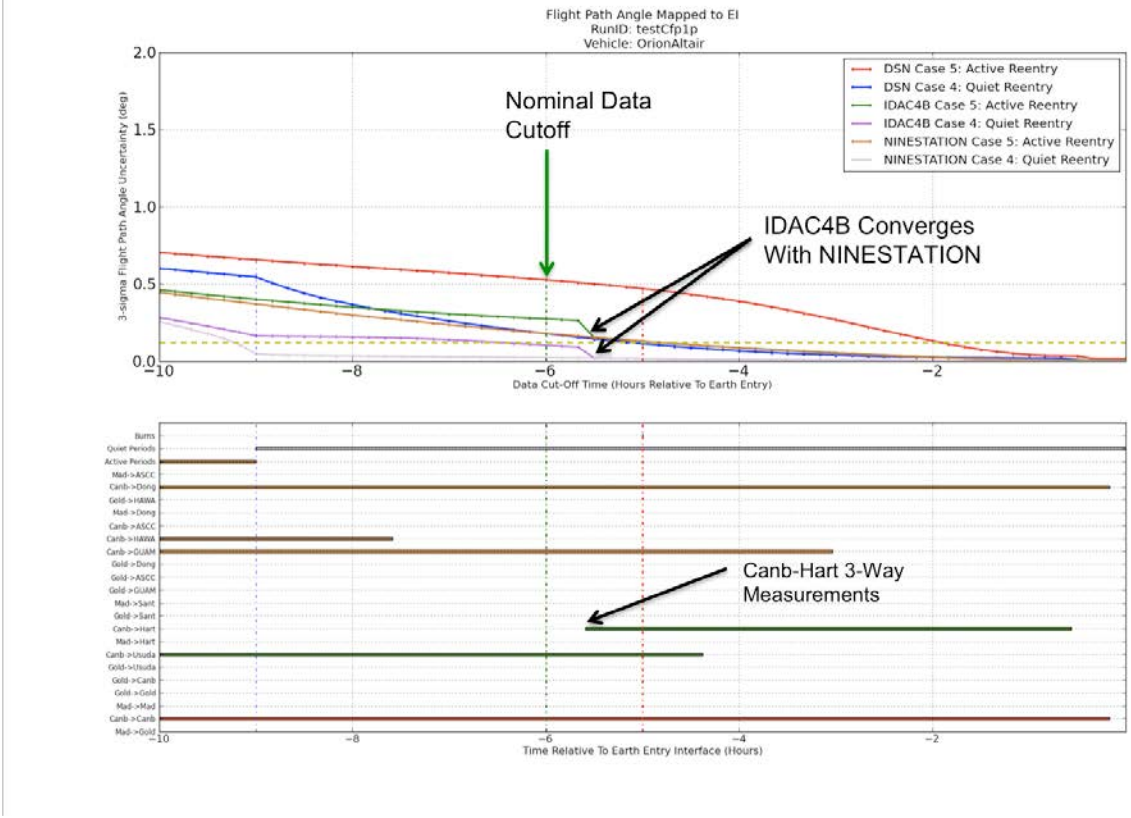

Figure 16: 3-Sigma EFPA Mapping From Various Data Cutoff Times For CFP-1P Radiometric Cases

The following conclusions can be drawn from this trade comparison:

1. DSN performance is invariant to geometry changes. The architecture lacks sufficient tracking to yield an acceptable EFPA dispersion.
2. IDAC4B performance is sensitive to variations in geometry. Additional tracking may be required to ensure compatibility with all potential trajectories.
3. The EFPA dispersion requirement cannot be met if active levels of FLAK are exerted after TCM7 data cutoff. Either the spacecraft must be required to meet a quiescent FLAK level or TCM7 must be moved closer to EI. Moving TCM7 closer to EI will require a larger delta-V budget.

B. Optical Tracking Results

1. CFP-1 Results

Recall that the goal of the optical tracking study is to study the performance of only the onboard camera system in an abort scenario where there is no Earth ground navigation support. Preliminary results from the CFP-1 optical navigation study indicate that a wide-angle camera will not provide sufficient navigation knowledge for safely returning to Earth in a "No Comm" contingency scenario. Since the contingency scenario is only concerned with survivable reentry, the precise skip entry profile will be abandoned in preference for a direct entry. The benchmark for these cases is raised to 0.5° (3σ). As seen in Figure 17, the wide-angle startracker yields EFPA dispersions exceeding the 0.5° benchmark for all cases. The wide-angle startracker comes closest to meeting the EFPA benchmark if observations are taken of GEO satellites. However, this assumes that the optical camera can be gimbaled at one-hour intervals to point toward GEO satellites. It also assumes that a very precise ephemeris will be preloaded on the spacecraft for orbiting objects in GEO. Another promising case involves observations of points along the Earth's limb. If no position uncertainty of the limb points is assumed, the wide-angle startracker is capable of yielding a 0.74° EFPA dispersion. If the limb point position uncertainty is assumed to be an observable white

noise stochastic, the EFPA dispersion rises slightly to 0.82°. However, it is likely that the limb point position uncertainty will not be observable due to systematic variations caused by weather patterns, time of day, time of season, and Sun cycle. These variations will make it difficult to produce consistent and usable navigation observables. If the limb point position uncertainty is modeled as a consider parameter, the EFPA dispersion result jumps to approximately 5°, which would certainly be inadequate for Earth entry. Lastly, optical tracking of lunar landmarks with a wide-angle camera performs poorly regardless of whether a fixed-axis or gimbaled-axis platform is used. At long ranges, the wide-angle camera does not provide enough resolution to obtain strong measurement observables and is not suitable for this application.

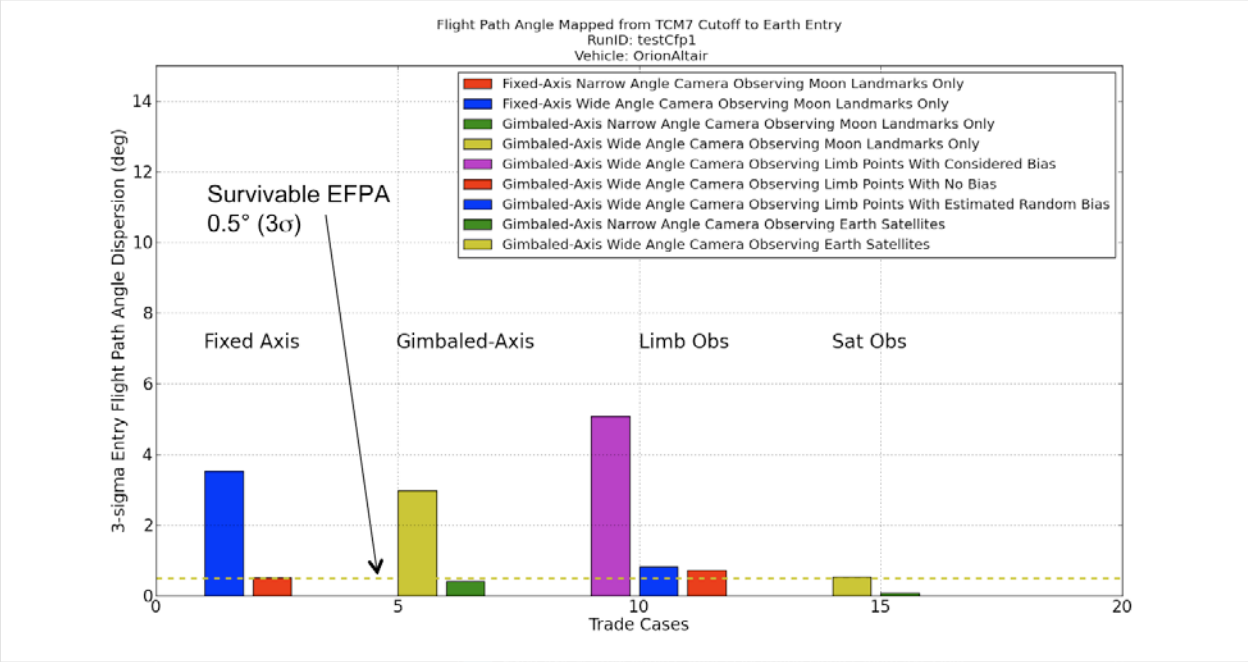

Figure 17: EFPA Dispersions For CFP-1 Optical Tracking Architectures

A narrow-angle camera, however, is shown to provide sufficient knowledge depending on the type of measurements taken and whether or not a gimbal is attached. Figure 18 clearly shows that use of the narrow-angle camera can provide an order of magnitude better navigation position determination than use of the wide-angle camera even though both cameras have equal visibility of sunlit optical targets throughout the scenario. A gimbaled-axis narrow-angle camera observing Earth-orbiting GEO satellites during Earth return achieves the best navigation performance. The performance of this case is so good that it potentially could meet the 0.12° EFPA requirement for the nominal skip entry. However, the assumptions associated with wide-angle GEO satellite observations still apply for the narrow-angle camera. The narrow angle only slightly satisfies the EFPA benchmark when taking observations of lunar landmarks on the return to Earth. There is no appreciable difference between results using a fixed-axis scan platform and a gimbaled-axis scan platform. The two hour imaging update prior to the TCM7 data cutoff enables the fixed-axis navigation knowledge to converge with the gimbaled-axis navigation state knowledge prior to EI targeting with TCM7, as seen in Figure 18. Although the range to the Moon is large during the critical moments prior to EI, the narrow angle camera provides enough resolution to observe small lunar features from long ranges. It is not as powerful as observing closer Earth orbiting objects, but lacks the measurement noise induced by a planetary atmosphere. Limb observations are not considered with a narrow-angle camera since the limb size begins to exceed the narrow-angle field of view several hours prior to TCM7.

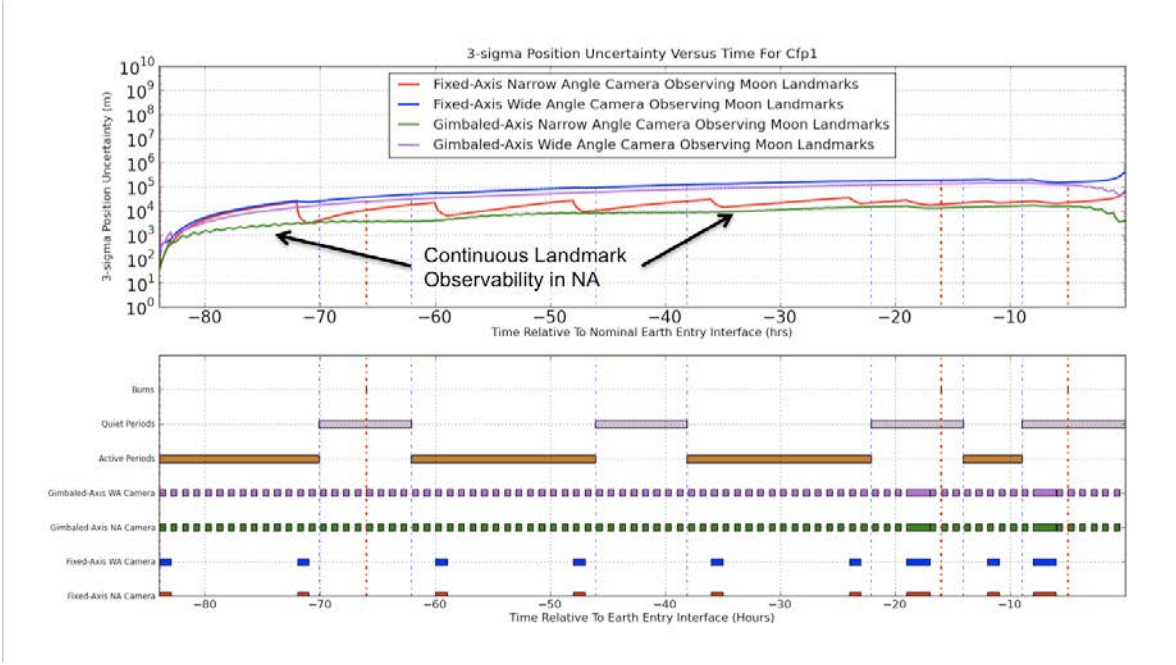

Figure 18: 3-Sigma Navigation Position Uncertainty For CFP-1 Cases Observing Moon Landmarks

Overall, the narrow-angle camera produces an EFPA dispersion of no greater than 0.5° (3σ) for all optical measurement cases. In contrast, the wide-angle camera can only produce a 0.55° EFPA dispersion at best, assuming it is mounted on a gimbaled-axis and contains high-fidelity ephemerides of GEO satellites.

The following conclusions can be drawn from this trade comparison:

1. The wide-angle startracker cannot meet the 0.5° benchmark, even under optimal conditions.
2. The narrow-angle camera satisfies the 0.5° benchmark with large margin when observing GEO satellites.
3. Lunar landmarks can provide powerful measurements for the narrow-angle camera, but provide weak observables for the wide-angle startracker during Earth return.
4. Limb observations may be extremely difficult to model due to atmospheric variations.

2. CFP-1P Results

Results from the CFP-1P scenario shown in Figure 19 indicate similar performance to the CFP-1 scenario. All wide-angle startracker cases exceed the 0.5° benchmark except for GEO satellite observations case, which yields an EFPA dispersion slightly below the 0.5° benchmark. Similar to the CFP-1 cases, all narrow-angle camera cases yield EFPA dispersions below the 0.5° benchmark, with the GEO satellite observations case yielding good enough performance to enable a nominal skip entry.

The only appreciable difference between the CFP-1 and CFP-1P cases is that the narrow-angle camera lacks observability of lunar landmarks for the first 30 hours of the CFP-1P case due to poor lighting conditions and a narrow field of view. Figure 20 depicts the growth in position uncertainty prior to EI-60 hours due to lack of measurements. However, once measurements begin in the narrow-angle camera, the navigation knowledge converges to similar levels seen in the CFP-1 cases. Since the measurement outage occurs prior to TCM7 data cutoff, there is no noticeable effect on EFPA dispersion results.

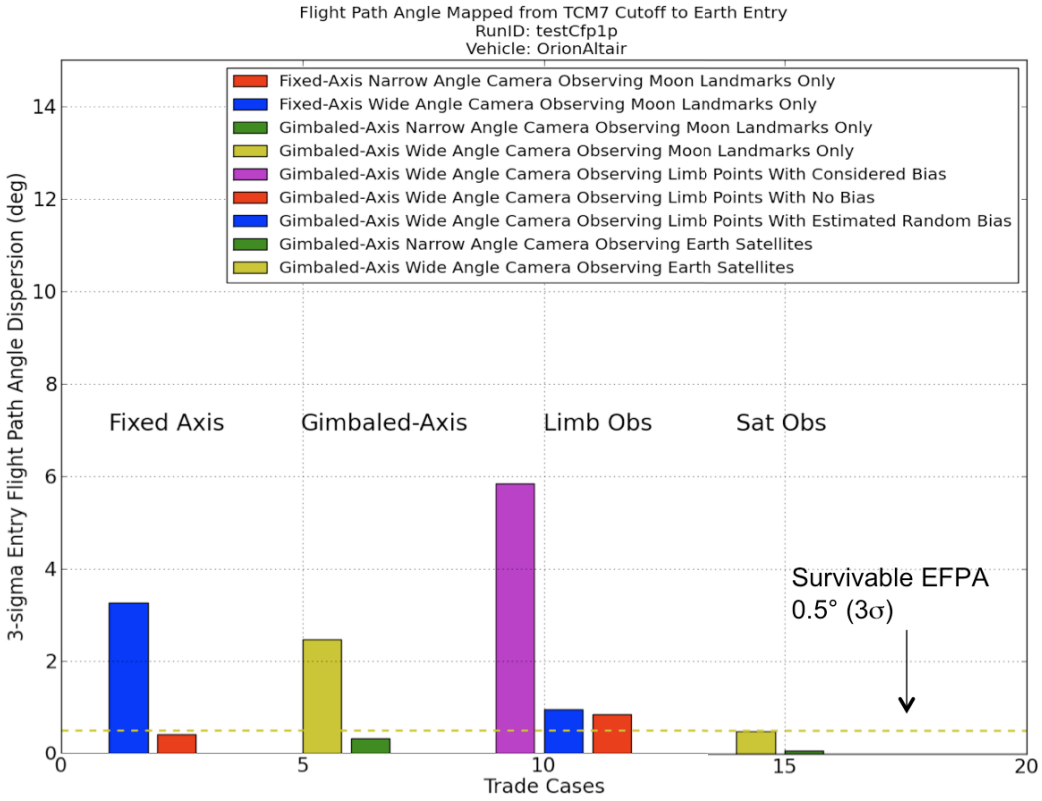

Figure 19: EFPA Dispersions For CFP-1P Optical Tracking Architectures

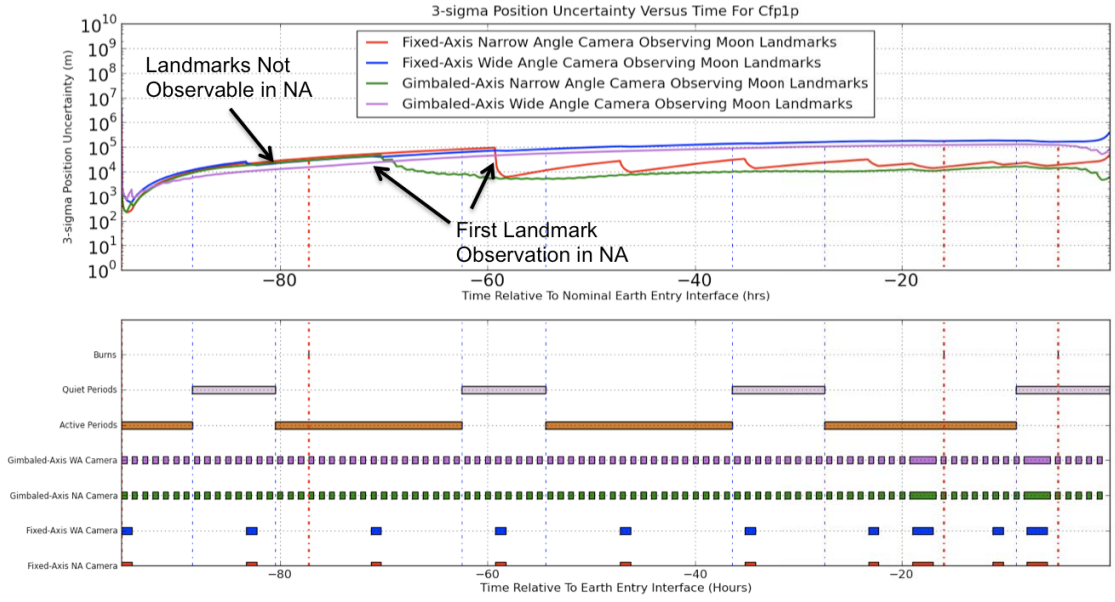

Figure 20: 3-Sigma Navigation Position Uncertainty For CFP-1P Moon Landmark Observations

The following conclusions can be drawn from this trade comparison:

1. The contingency Earth return scenario is relatively invariant to geometric variations.
2. The EFPA dispersion is most sensitive to the strength of the measurements, which is highly dependent on the camera resolution.

IX. Conclusion

The Earth return problem for manned spacecraft is a challenging one. An optimal set of radiometric tracking stations must satisfy the navigation needs of an endless number of spacecraft trajectories with uncertain process noise characteristics. At the same time, manned missions continue to have less tolerance for risk and require onboard navigation systems, such as optical navigation, for contingency operations. While the current work shows promise that solutions do exist, future work will have to rigorously investigate sensitivities to geometry variations, produce higher-fidelity FLAK models, and perform trades between TCM7 delta-V and EFPA performance.

Acknowledgments

This work was carried out at the Jet Propulsion Laboratory, California Institute of Technology, under contract with the National Aeronautics and Space Administration. The authors would like to thank Joe Guinn for his support and Ed Riedel for his insight into the optical tracking problem. The authors would also like to thank Michelle Guevara, Joe Wu, and Ted Drain for their support regarding the MONTE software interface.

References

[1] Bush, G.W., "The Vision For Space Exploration," NASA. February 2004.
[2] D'Souza, C., Crain, T., Clark, F., Getchius J., "Orion Cislunar Guidance and Navigation," *AIAA Guidance, Navigation and Control Conference and Exhibit,* AIAA-07-6678, Hilton Head, S.C., August 2007.
[3] D'Souza, C., Getchius, J., Holt, G., Moreau, M., "Lunar Navigation Architecture Design Considerations," *AAS Guidance And Control Conference,* AAS 09-096, Breckenridge, Colorado, February 2009.
[4] Lee, T., Long, A., Berry, K., Carpenter, R., Moreau, M., Holt, G., "Navigating the Return Trip from the Moon Using Earth-Based Ground Tracking and GPS," *AAS Guidance And Control Conference,* AAS 09-096, Breckenridge, Colorado, February 2009.
[5] Zanetti, R., "Autonomous Mid-Course Navigation for Lunar Return," FltDyn-CEV-08-139, August 8, 2008.
[6] D'Souza, C., "Process Noise for Lunar Missions," EG-CX-06-3, April 19, 2006.
[7] Gates, C. R., "A Simplified Model of Midcourse Maneuver Execution Errors," Jet Propulsion Laboratory, Technical Memorandum No. 32-504, October 15, 1963.
[8] Ely, T., "Modeling Dynamic Stochastic Accelerations with Either Gaussian or Poisson White Noise," Jet Propulsion Laboratory, September 25, 2009.
[9] Bierman, G. J., *Factorization Methods for Discrete Sequential Estimation,* Academic Press, New York, 1977, Chaps. I-VIII.